The Astrophysical Journal, 890:6 (8pp), 2020 February 10 https://doi.org/10.3847/1538-4357/ab6218
© 2020. The American Astronomical Society. All rights reserved.

A Curious Case of Circular Polarization in the 25 GHz Methanol Maser Line toward OMC-1

A. P. Sarma[1] and E. Momjian[2]
[1] Department of Physics and Astrophysics, DePaul University, 2219 N. Kenmore Ave., Byrne Hall 211, Chicago, IL 60614, USA; asarma@depaul.edu
[2] National Radio Astronomy Observatory, P.O. Box O, Socorro, NM 87801, USA; emomjian@nrao.edu
Received 2019 September 4; revised 2019 December 9; accepted 2019 December 12; published 2020 February 6

Abstract

We report the detection of a circular polarization signature in the Stokes *V* profile of a 25 GHz Class I CH_3OH maser toward the high-mass star-forming region OMC-1. Such a feature usually constitutes a detection of the Zeeman effect. If due to a magnetic field in OMC-1, this would represent the first detection and discovery of the Zeeman effect in the 25 GHz Class I CH_3OH maser. The feature in Stokes *V* is detected in two observations with different angular resolutions taken eight years apart with the Very Large Array; for our 2009 *D*-configuration observations, the fitted value for $z\,B_{\rm los}$ is 152 ± 12 Hz, where z is the Zeeman splitting factor and $B_{\rm los}$ is the line-of-sight magnetic field. For our 2017 *C*-configuration observations, the fitted value for $z\,B_{\rm los}$ = 149 ± 19 Hz, likely for the same maser spot. These correspond to $B_{\rm los}$ in the range 171–214 mG, depending on which hyperfine transition is responsible for the maser line. While these $B_{\rm los}$ values are high, they are not implausible. If the magnetic field increases in proportion to the molecular hydrogen density in shocked regions, then our detected fields predict values for the pre-shock magnetic field that are in agreement with observations. With $B_{\rm los}$ = 171–214 mG, the magnetic energy in the post-shocked regions where these 25 GHz Class I CH_3OH masers occur would dominate over the kinetic energy density and be at least of the order of the pressure in the shock, implying that the magnetic field would exert significant influence over the dynamics of these regions.

Unified Astronomy Thesaurus concepts: Interstellar medium (847); Astrophysical masers (103); Interstellar magnetic fields (845); Interstellar molecules (849); High resolution spectroscopy (2096); Star formation (1569); Star forming regions (1565); Polarimetry (1278)

1. Introduction

Of the well known Class I methanol (CH_3OH) maser transitions, the $J_2 - J_1$ E series of maser lines near 25 GHz are different because of their inversion mechanism. Unlike Class I CH_3OH maser transitions at 36, 44, 84, and 95 GHz, the $J_{k=2} - J_{k=1}$ lines responsible for CH_3OH maser transitions near 25 GHz depend on $\Delta k \neq 0$ to build up the population in the $k = 2$ and $k = 1$ E-type methanol ladders (Leurini et al. 2016). Like all the other Class I CH_3OH masers, however, masers near 25 GHz also arise in outflows in star-forming regions, where collisional pumping creates the necessary population inversion (Menten 1993). Therefore, they enable us to observe such regions at high angular resolution. In particular, high-mass star-forming regions must be observed at high angular resolution because high-mass stars usually form in clusters, and much remains to be known about how they form (Motte et al. 2018). Moreover, both 36 and 44 GHz Class I CH_3OH masers trace the Zeeman effect (Sarma & Momjian 2009; Momjian & Sarma 2019), which constitutes the most direct method to measure magnetic fields in star-forming regions (e.g., Troland & Crutcher 2008). The ability to detect the Zeeman effect in 25 GHz Class I CH_3OH maser lines would open a new window into the measurement of magnetic fields in star-forming regions. Magnetic fields are known to play an important role during several stages of the star formation process, but the details remain a matter of debate, in part due to the scarcity of observational data in the high-density environments close to the forming star (Crutcher 2012; Krumholz & Federrath 2019).

The Orion Molecular Cloud 1 (OMC-1) holds the distinction of hosting, to date, the brightest masers in the 25 GHz Class I CH_3OH species (Barrett et al. 1971). OMC-1 is a ridge of dense molecular gas that lies behind the ionized region caused by the OB stars of the Trapezium cluster in the Orion Nebula (e.g., Pabst et al. 2019). With an extent of ∼2 pc along the north–south direction, OMC-1 is near the center of the integral-shaped filament that was mapped in ^{13}CO by Bally et al. (1987). This integral-shaped filament, at the northern end of the Orion A giant molecular cloud, is a clumpy, narrow (<1′, or 0.2 pc) ridge of emission that extends in the north–south direction for over 50′ (7 pc), with fainter filaments and clumps extending orthogonal to the ridge for several arcminutes (Johnstone & Bally 1999). Being part of the nearest high-mass star-forming region at a distance of 388 ± 5 pc (Kounkel et al. 2017), OMC-1 has been observed extensively at optical, infrared, radio, etc. wavelengths in both continuum and spectral lines (see, e.g., Genzel & Stutzki 1989; Bally 2008; Hacar et al. 2018, and references therein). OMC-1 contains the well-known Becklin–Neugebauer (BN) object (Becklin & Neugebauer 1967) and the Kleinmann–Low (KL) nebula (Kleinmann & Low 1967). Centered near Orion-KL is a wide-angle, high-velocity outflow oriented in a northwest–southeast direction (Erickson et al. 1982). When this high-velocity outflow slams into ambient gas, it produces shocks; such shocked regions can be imaged in the molecular hydrogen $\nu = 1 - 0\ S(1)$ emission line, as has been done for OMC-1 (Beckwith et al. 1978). It is in such shocked regions that CH_3OH masers are formed; in OMC-1, the 25 GHz Class I CH_3OH masers are distributed along an arc that runs from northwest to southeast (Johnston et al. 1992).

In this paper, we report the presence of a circular polarization signature in the Stokes *V* profile of a 25 GHz Class I CH_3OH maser line toward OMC-1 that is usually interpreted as a

detection of the Zeeman effect. If this Stokes *V* profile is truly due to a magnetic field, then the work reported in this paper would represent the first detection of the Zeeman effect in the 25 GHz Class I CH_3OH maser line. In Section 2, we describe the observational setup and the data reduction process. In Section 3, we present our results, along with a description of the analysis of data for the Zeeman effect. These results are discussed in Section 4, and our conclusions are presented in Section 5.

2. Observations and Data Reduction

We present results from two separate epochs of observations on the 25 GHz ($5_2 - 5_1$ E) Class I CH_3OH maser line (rest frequency 24.959 GHz) toward the star-forming region OMC-1. Observations in the first epoch were carried out with the pre-upgrade Very Large Array (VLA)[3] on 2009 October 22 in a single 3 hr session in the *D*-configuration (maximum baseline of ∼1 km). In 2009, the VLA was still undergoing a major upgrade through the Expanded VLA (EVLA) project. While the observations used all the 21 antennas retrofitted to the EVLA standards and excluded the old-style antennas, the data were correlated using the old VLA correlator, delivering a bandwidth of 1.56 MHz with 255 spectral channels and dual polarization products (RR, LL). This resulted in a channel spacing of 6.1 kHz, which corresponds to 0.073 km s^{-1} at the observed frequency. At the time, the use of EVLA antennas with the old correlator in spectral line observations introduced aliasing that impacted the lower 0.5 MHz of the bandwidth. Therefore, the 25 GHz CH_3OH maser line was centered in the upper half of the 1.56 MHz bandwidth. Observations in the second epoch were carried out with the post-upgrade VLA, formally the Karl G. Jansky VLA, on 2017 June 11, also in a single 3 hr session but in the more extended *C*-configuration (maximum baseline of 3.4 km). The Wideband Interferometric Digital ARchitecture correlator, which is the post-upgrade VLA correlator, was configured to deliver a single 4 MHz sub-band with dual polarization products (RR, LL) and 1024 spectral channels. The resulting channel spacing was 3.91 kHz, corresponding to 0.047 km s^{-1} at the observed frequency. In both epochs, the source J0542+4951 (3C147) was observed to calibrate the absolute flux density scale. In the higher angular resolution observations of 2017, we employed phase referencing in part of the observing session in order to derive the absolute positions of the masers in the target source. The phase calibrator was the nearby source J0541−0541, and the phase referencing cycle time was five minutes. All the data reduction steps, calibration, imaging, and deconvolution, were carried out independently for each observing epoch using the Astronomical Image Processing System (AIPS; Greisen 2003) of the National Radio Astronomy Observatory. The spectral channel with the brightest maser emission was split off, and self-calibrated first in phase, then in both phase and amplitude, and imaged in a succession of iterative cycles. The final self-calibration solutions were then applied to the full spectral-line uv data sets of OMC-1 from each epoch. In order to improve the signal-to-noise of the higher angular resolution data set of 2017, the Stokes *I* and *V* image cubes were constructed by averaging every two channels, resulting in a velocity spacing of 0.094 km s^{-1}. Note that AIPS calculates the Stokes parameter *I* as the average of the right circular polarization (RCP) and left circular polarization (LCP), so that $I = (\mathrm{RCP} + \mathrm{LCP})/2$, whereas Stokes *V* is calculated by AIPS as half the difference between RCP and LCP, so that $V = (\mathrm{RCP} - \mathrm{LCP})/2$; henceforth, all values of *I* and *V* are based on this implementation in AIPS. Also note that RCP is defined here in the standard radio convention, in which it is the clockwise

[3] The National Radio Astronomy Observatory is a facility of the National Science Foundation operated under cooperative agreement by Associated Universities, Inc.

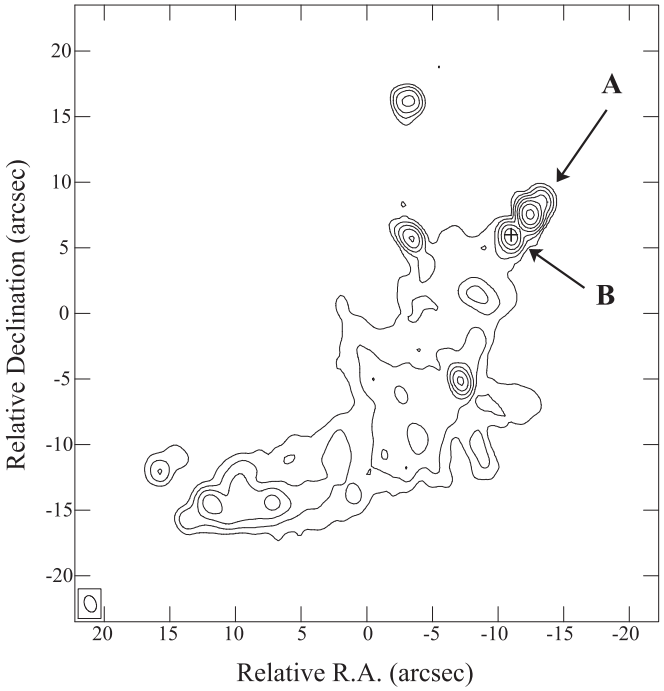

Figure 1. Velocity-integrated image of the 25 GHz Class I CH_3OH masers toward OMC-1 from our 2017 VLA *C*-configuration observations. The contours are at (0.5, 1, 2, 4, 8, 16, 32) × 0.4 Jy $beam^{-1}$ km s^{-1}. The FWHM of our synthesized beam is $1\farcs30 \times 0\farcs89$, and is shown as an inset in the bottom left. The (0, 0) position in this image corresponds to $\alpha = 05^{h}35^{m}14\fs455$, $\delta = -05°22'31\farcs40$ (J2000). The parameters of masers A and B marked in this figure are given in Table 2. The plus sign marks the position in maser B toward which we measured the Zeeman effect.

Table 1
Parameters for VLA Observations

Parameter	2009 Observations Value	2017 Observations Value
Date	2009 Oct 22	2017 Jun 11
Configuration	*D*	*C*
R.A. of field center (J2000)	$05^{h}35^{m}14\fs02$	$05^{h}35^{h}14\fs02$
Decl. of field center (J2000)	$-5°22'30\farcs9$	$-5°22'30\farcs9$
Total bandwidth (MHz)	1.56	4.00
No. of channels	255	1024
Channel spacing (km s^{-1})	0.073	0.094 [a]
Approx. time on source (hr)	2.4	2.3
Rest frequency (MHz)	24959.079	24959.079
FWHM of synthesized beam	$3\farcs34 \times 2\farcs71$ P.A. = $-2\fdg61$	$1\farcs30 \times 0\farcs89$ P.A. = $19\fdg47$
Line rms noise (mJy $beam^{-1}$)[b]	4.0	2.2

Notes.
[a] Image cubes were made by averaging every two channels.
[b] The line rms noise was measured from the Stokes *I* image cube using maser line-free channels.

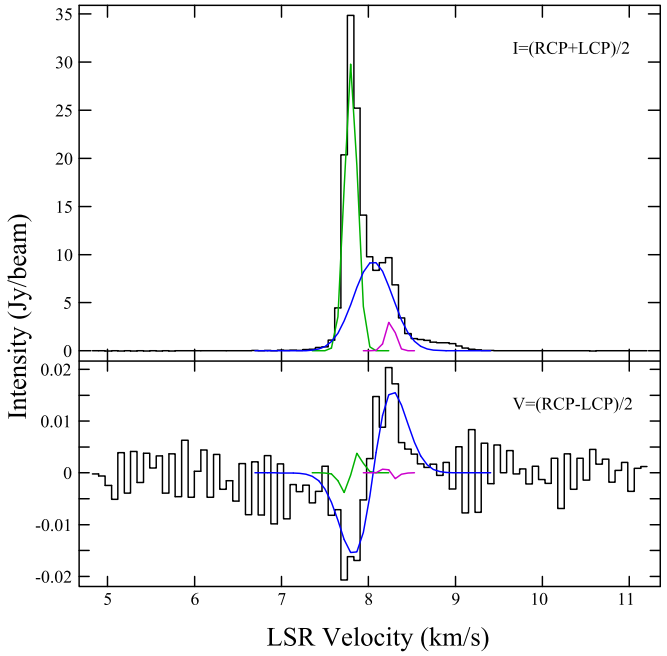

Figure 2. Stokes *I* (upper panel: black histogram-like line) and Stokes *V* (lower panel: black histogram-like line) profiles from our 2009 observations toward the maser spot in OMC-1 listed as A+B in Table 2. The green, blue, and magenta curves in the upper panel show the Gaussian components that we fitted to the Stokes *I* profile (components 1–3, respectively, for the maser listed as A+B in Table 2). The green, blue, and magenta curves in the lower panel are the derivatives of the corresponding colored curves in the upper panel, scaled by the fitted value of $z\,B_{\rm los}$ for each curve, obtained from our fitting procedure described in Section 3.

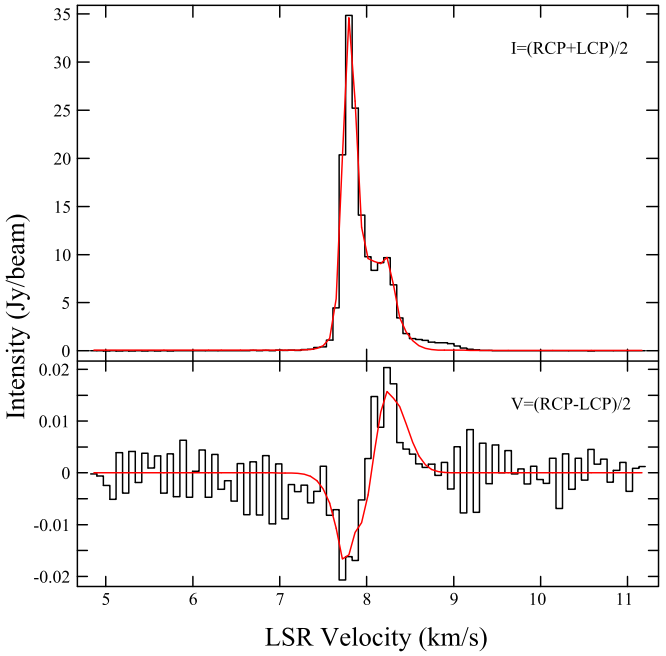

Figure 3. Stokes *I* (upper panel: black histogram-like line) and Stokes *V* (lower panel: black histogram-like line) profiles from our 2009 observations toward the maser spot in OMC-1 listed as A+B in Table 2. The red curve in the upper panel is the sum of the three Gaussian components shown by green, blue, and magenta curves in the upper panel of Figure 2 (and listed in Table 2) that we fitted to the Stokes *I* profile. The red curve superposed on the Stokes *V* profile in the lower panel is the sum of the green, blue, and magenta curves shown in the lower panel of Figure 2; that is, it is the sum of the scaled derivatives of the Gaussian components fitted to the Stokes *I* profile, where each of the three derivative profiles has been scaled appropriately by the fitted value of $z\,B_{\rm los}$, as described in the caption to Figure 2.

Table 2
Fitted Parameters for OMC-1 Masers

Maser	Component	Intensity (Jy beam^{-1})	Center Velocity[a] (km s^{-1})	Velocity Linewidth[b] (km s^{-1})
		2009 observations		
A+B	1	29.84 ± 0.46	7.799 ± 0.001	0.173 ± 0.003
	2[c]	**9. 27 ± 0.20**	**8. 054 ± 0.013**	**0. 529 ± 0.016**
	3	3.13 ± 0.36	8.254 ± 0.006	0.127 ± 0.019
		2017 observations		
A	1	54.30 ± 1.30	7.776 ± 0.001	0.162 ± 0.002
	2	14.56 ± 1.14	7.862 ± 0.008	0.293 ± 0.007
B	1	12.10 ± 0.91	8.210 ± 0.002	0.234 ± 0.008
	2[c]	**4. 47 ± 0.61**	**8. 084 ± 0.039**	**0. 487 ± 0.033**
	3	0.66 ± 0.15	8.649 ± 0.088	0.395 ± 0.130

Notes.
[a] The center velocity values are with respect to the LSR.
[b] The velocity linewidth was measured at FWHM.
[c] The components marked in bold (component 2 for maser A+B from our 2009 observations, and component 2 for maser B from our 2017 observations) are those in which we have significant detection for $b = z\,B_{\rm los}$.

rotation of the electric vector when viewed along the direction of wave propagation. Table 1 summarizes the parameters of the VLA observations and the corresponding synthesized beam-widths and other parameters for each observing epoch.

3. Results

The 25 GHz Class I CH_3OH masers toward OMC-1 are arranged in an arc that spans roughly a quarter of a circle and runs from northwest to southeast; this is shown in Figure 1, and corresponds well with Johnston et al. (1992). Figure 1 is a velocity-integrated image taken from our VLA *C*-configuration observations; in our *D*-configuration observations of 2009, the maser marked with a plus (+) sign and the maser to its northwest (masers B and A respectively in Figure 1) were observed as one (unresolved) maser feature. The upper panel of Figure 2 shows the Stokes *I* profile toward this maser from our *D*-configuration observations in 2009. We fitted this profile with three Gaussian components; they are also displayed in the upper panel of Figure 2. The intensity, velocity at line center with respect to the local standard of rest (LSR), and velocity linewidth measured at full width at half maximum (FWHM) of each of the three components are given in Table 2, where we have listed the maser spot as A+B in view of our higher-resolution observations carried out in 2017 (and explained in more detail below). Of the three components for maser A+B in our 2009 observations, the strongest (29.8 Jy beam^{-1}) is centered at an LSR velocity of 7.80 km s^{-1}, component 2 (9.3 Jy beam^{-1}) is centered at 8.05 km s^{-1}, and component 3 (3.1 Jy beam^{-1}) is centered at 8.25 km s^{-1}. Components 1 and 3 are quite narrow with FWHM velocity linewidths of 0.17 km s^{-1} and 0.13 km s^{-1} respectively, whereas component 2 is broader with a FWHM linewidth of 0.53 km s^{-1}.

The composite profile obtained from the sum of these three Gaussian components is shown in the upper panel of Figure 3.

In our higher angular resolution (VLA *C*-configuration) observations of 2017, the maser spot A+B from our 2009 observations was resolved into two distinct spots, both of which have additional velocity components; we have labeled the stronger maser spot as A and the lower intensity spot as B (see Figure 1). We fitted maser A from our 2017 observations with two Gaussian components. Component 1 (54 Jy beam^{-1}) is centered at LSR velocity 7.78 km s^{-1} and has a velocity linewidth of 0.16 km s^{-1}. On the basis of the velocity at line center and the FWHM linewidth, component 1 of maser A from our 2017 observations likely matches component 1 of maser A+B from our 2009 observations. Maser A in our 2017 observations also has a second weaker component (14.6 Jy beam^{-1}) at an LSR velocity of 7.86 km s^{-1} and a FWHM velocity linewidth of 0.29 km s^{-1}. Meanwhile, we fitted the lower-intensity maser spot B from our 2017 observations with three Gaussian components (Table 2); the Stokes *I* profile for maser B, together with these three Gaussian components, is shown in the upper panel of Figure 4. The strongest of these three velocity components (12.1 Jy beam^{-1}) is at an LSR velocity of 8.21 km s^{-1}, component 2 is at 8.08 km s^{-1}, and component 3 is at 8.65 km s^{-1}. The composite profile obtained from the sum of these three Gaussian components is shown in the upper panel of Figure 5.

The Stokes *V* profile of maser A+B from our 2009 observations (lower panel of Figures 2 and 3) reveals an S-shaped structure that is usually taken to be a detection of the Zeeman effect (also see the discussion in Section 4 below); so does the Stokes *V* profile from our 2017 observations (lower panel of Figures 4 and 5). No other compact maser spots in this field show any such feature. Whenever an S-shaped feature is observed in Stokes *V*, the magnetic field strength is usually determined by fitting a numerical frequency derivative of the Stokes *I* spectrum to the Stokes *V* spectrum; details are in, e.g., Momjian & Sarma (2017). The Stokes *V* profile is usually fit simultaneously to the derivative of the *I* profile and a scaled replica of the *I* profile itself via the equation (Troland & Heiles 1982; Sault et al. 1990)

$$V = aI + \frac{b}{2}\frac{dI}{d\nu}. \quad (1)$$

The scaled replica of the *I* spectrum is included in the fit to account for small calibration errors in RCP versus LCP; for all results reported in this paper, $a \lesssim 10^{-3}$. The magnetic field values are contained in the fit parameter *b*, which is equal to $z\,B_{\rm los}$, where *z* is the Zeeman splitting factor, and $B_{\rm los}$ is the line-of-sight (LOS) magnetic field strength (assuming, of course, that the signature in Stokes *V* is due to the magnetic field in the region; see Section 4.2). We used the AIPS task ZEMAN (Greisen 2015) to carry out the fit in Equation (1). This task allows multiple Gaussian components in *I* to be fitted simultaneously to *V*, with each Gaussian component fitted for a different *b*, and hence a different LOS magnetic field strength. For the three Gaussian components of maser A+B from our 2009 observations (listed in Table 2, and shown in the upper panel of Figure 2), the derivative profiles scaled by the respective values fitted for $b = z\,B_{\rm los}$ are each shown in the lower panel of Figure 2; the composite profile obtained by adding together these three scaled derivative profiles is shown in the lower panel of Figure 3. Of these three components for maser A+B from our 2009 observations, only component 2 showed a significant fit, with the fitted value given by $z\,B_{\rm los} = 152 \pm 12$ Hz. Following customary practice in the field of Zeeman observations, we consider fits to be significant only if the ratio of fitted value to the fitted error is at the 3σ level or greater. Meanwhile, for the three Gaussian components of maser B from our 2017 observations (listed in Table 2, and shown in the upper panel of Figure 4), the derivative profiles scaled by the respective fitted values for $B_{\rm los}$ are each shown in the lower panel of Figure 4, and the composite profile is shown in the lower panel of Figure 5. Only component 2 of maser B from our 2017 observations showed a significant fit, with the fitted value given by $z\,B_{\rm los} = 149 \pm 19$ Hz. Since component 2 of maser A+B from our 2009 observations and component 2 of maser B from our 2017 observations are very likely the same maser spot (see Section 4.1), this is a remarkable coincidence in $B_{\rm los}$ over observations taken eight years apart.

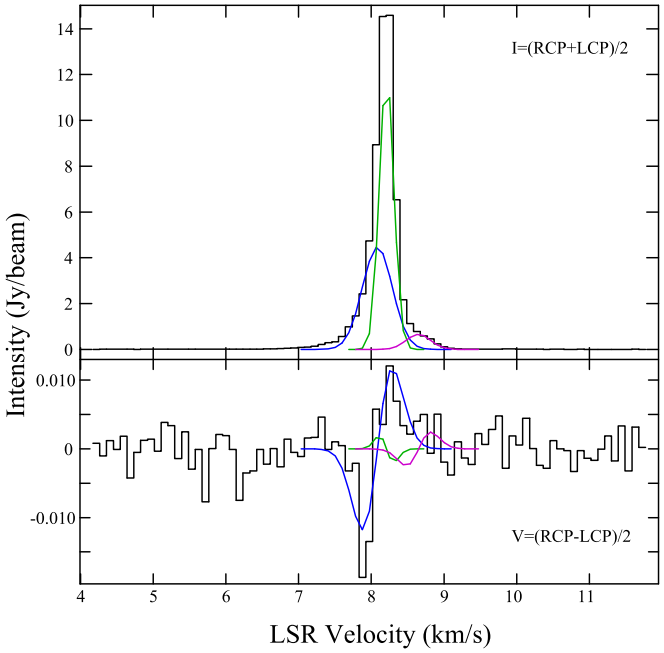

Figure 4. Stokes *I* (upper panel: black histogram-like line) and Stokes *V* (lower panel: black histogram-like line) profiles from our 2017 observations toward the maser in OMC-1 listed as B in Table 2. The green, blue, and magenta curves in the upper panel show the Gaussian components that we fitted to the Stokes *I* profile (components 1–3, respectively, for maser B in Table 2). The green, blue, and magenta curves in the lower panel are the derivatives of the corresponding colored curves in the upper panel, scaled by the fitted value of $z\,B_{\rm los}$ for each curve, obtained from our fitting procedure described in Section 3.

Extracting the value of $B_{\rm los}$ from the fit parameter *b* in Equation (1) requires knowing the value of the Zeeman splitting factor *z*. This is not easy, since CH_3OH maser lines may be comprised of one or more hyperfine transitions. Lankhaar et al. (2018) derived the values of *z* for a wide array of methanol maser lines by doing quantum mechanical calculations. For the 25 GHz $5_2 - 5_1$ E Class I CH_3OH maser line that we observed, they list the values of *z* for eight hyperfine components. Four of these have $|z|$ between 0.7 and 0.9 Hz mG^{-1}, and the corresponding values of $B_{\rm los}$ are listed in Table 3; they range from 171 to 214 mG. This is 3–4 times higher than the largest $B_{\rm los}$ we have measured at 44 GHz

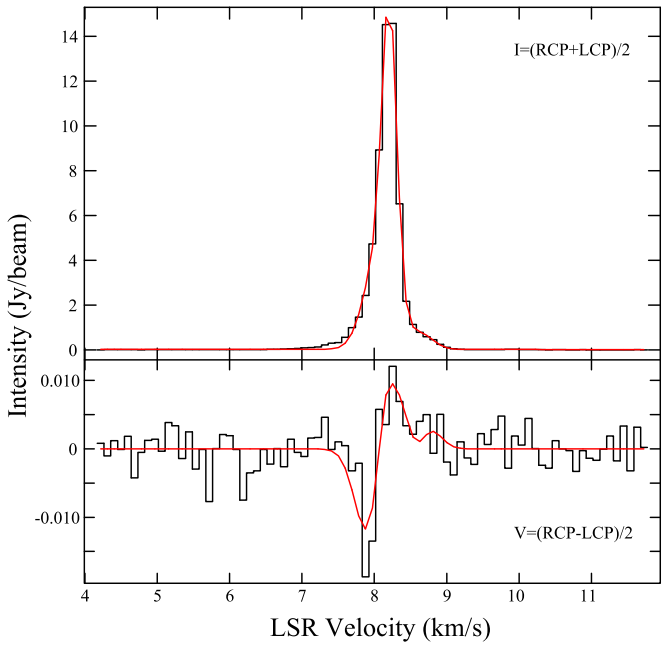

Figure 5. Stokes *I* (upper panel: black histogram-like line) and Stokes *V* (lower panel: black histogram-like line) profiles from our 2017 observations toward the maser in OMC-1 listed as B in Table 2. The red curve in the upper panel is the sum of the green, blue, and magenta Gaussian components shown in Figure 4 (and listed in Table 2) that we fitted to the Stokes *I* profile. The red curve superposed on the Stokes *V* profile in the lower panel is the sum of the three colored curves shown in the lower panel of Figure 4; that is, it is the sum of the scaled derivatives of the Gaussian components fitted to the Stokes *I* profile, where each of the three derivative profiles has been scaled appropriately by the fitted value of $z\,B_{\rm los}$, as described in the caption to Figure 4.

Table 3
Magnetic Field Values

			2009 observations ($z\,B_{\rm los} = 152 \pm 12$ Hz)	2017 observations ($z\,B_{\rm los} = 149 \pm 19$ Hz)
$F_{\rm up}$[a]	$F_{\rm down}$[a]	$\lvert z\rvert$ (Hz mG^{-1})	$B_{\rm los}$ (mG)	$B_{\rm los}$ (mG)
6	6	0.708	214 ± 17	211 ± 27
4	4	0.873	174 ± 14	171 ± 22
6	6	0.732	207 ± 17	204 ± 26
4	4	0.864	175 ± 14	173 ± 22

Note.
[a] The notation for hyperfines is explained in Lankhaar et al. (2018). Briefly, for the 25 GHz $5_2 - 5_1$ E Class I CH_3OH masers, there are hyperfine states with $F = J$ and $F = J \pm 1$, with four levels for the former, and two each for the latter. Since $J = 5$ for the 25 GHz line, the possible values for $F_{\rm up}$ are 6, 5, 4, with four levels corresponding to $F_{\rm up} = 5$, two levels corresponding to $F_{\rm up} = 6$, and two levels for $F_{\rm up} = 4$; likewise for $F_{\rm down}$. The strongest hyperfine transitions are for $\Delta F = 0$. Thus, we have eight hyperfine transitions, of which four are listed here. The other four hyperfine transitions are not listed in this table because the $B_{\rm los}$ values calculated from them are unreasonably high (Section 3).

(Momjian & Sarma 2017), but not implausibly high (see the discussion in Section 4.3). The other four hyperfines have $\lvert z\rvert$ values in the range 0.02–0.06 Hz mG^{-1}; corresponding $B_{\rm los}$ values would be 10–50 times higher than 171 mG, too high for the regions traced by these 25 GHz CH_3OH masers, so we have not included them in Table 3 (also see Section 4.3). In other words, we can rule out that the hyperfines with $\lvert z\rvert = 0.02$–0.06 are

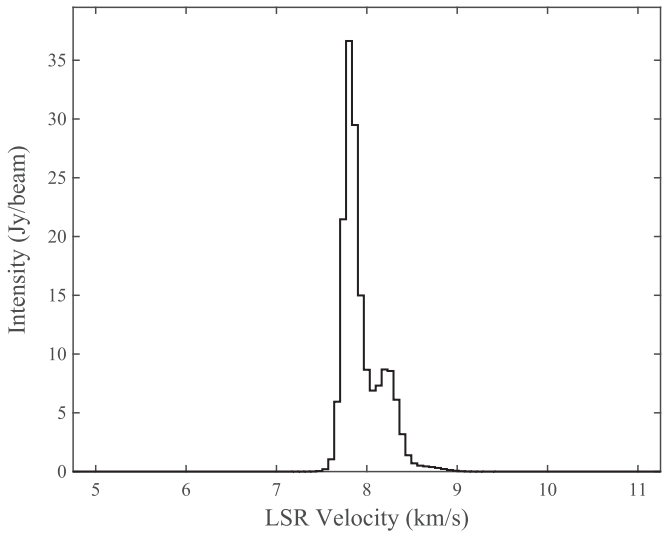

Figure 6. Composite Stokes *I* profile obtained by adding together the five fitted Gaussian components (two for maser A, three for maser B) listed in Table 2 for our 2017 *C*-configuration observations, and scaling by the ratio of intensities as described in Section 4.1. This composite spectrum is strikingly similar to the observed Stokes *I* profile from our 2009 *D*-configuration observations (see the upper panel of Figure 2), even picking up the very low-intensity extension past 8.5 km s^{-1}.

responsible for the maser transition being observed. We note also that we have ignored the sign of z in finding values for $B_{\rm los}$. Two of the four z values listed in Table 3 have negative signs in Lankhaar et al. (2018); by convention, a positive value for $B_{\rm los}$ (when z is positive) has meant that the LOS magnetic field is pointing away from the observer. Since z has mixed signs in the treatment of Lankhaar et al. (2018), and it is not clear which hyperfine is masing to create the population inversion for the 25 GHz line, we would like to avoid any comment on the sign of $B_{\rm los}$.

4. Discussion

The 25 GHz Class I CH_3OH masers in OMC-1 are the brightest masers of this species discovered to date. If the signature observed in Stokes *V* is due to magnetic fields in OMC-1, then this would represent the first detection of the Zeeman effect in the 25 GHz CH_3OH maser line.

4.1. Maser Spots

We fitted the maser labeled as A+B in our 2009 VLA *D*-configuration observations with three Gaussian components in velocity (Table 2). This maser was resolved into two sources in our 2017 VLA *C*-configuration observations; we fitted the stronger of these (maser A) with two Gaussian components in velocity, and the other (maser B) with three components (Table 2). In fitting Gaussian components to observed spectral line profiles, one acknowledges that the components themselves may not represent physical structures, but are the best decomposition of the observed spectral line. Still, it is worth checking if the five Gaussian components fitted to the 2017 *C*-configuration spectral lines (two components for maser A and three for maser B) are consistent with the profile observed with the *D*-configuration of the VLA in 2009. In order to carry out this check, we added together all five profiles in velocity space and generated a composite profile. This was then scaled by the ratio of the intensity of component 1 of maser A+B

from our 2009 observations to the intensity of component 1 of maser A from our 2017 observations (see Table 2). The result is shown in Figure 6, and matches remarkably well with our 2009 *D*-configuration observations, for which the Stokes *I* profile is shown in the upper panel of Figure 2 (and Figure 3), including even the very low-intensity wing at LSR velocities beyond 8.5 km s^{-1}. This increases the likelihood that the fitted velocity components correspond to actual maser spots in OMC-1. We have already stated above that component 1 of maser A+B from our 2009 observations is likely the same as component 1 of maser A in our 2017 observations. By comparing the $v_{\rm LSR}$ and FWHM velocity linewidth (Table 2), we conclude also that component 2 of maser A+B from our 2009 observations is likely the same as component 2 of maser B in our 2017 observations. The identification of these masers spots from our 2009 and 2017 observations as being likely the same is important because they are the maser spots in which we have a significant Zeeman detection, assuming the signature in the Stokes *V* profile is due to magnetic fields in OMC-1.

4.2. Instrumental Considerations and Non-Zeeman Interpretation

Structure in the Stokes *V* profile can also be caused by instrumental effects and processes other than the Zeeman effect. A velocity gradient across an extended source could produce a Stokes *V* profile due to the beam squint similar to that caused by the Zeeman effect. This appears unlikely in our current observations, since masers are point sources confined to a narrow velocity range. Another effect to consider is that in masers having high linear polarization to begin with, the linear polarization vector could rotate as the signal propagates along the LOS due to changes in the orientation of the magnetic field. This would cause a circular polarization signature in the signal received at the telescope (Wiebe & Watson 1998). Although no measurements of the linear polarization are available for the 25 GHz CH_3OH masers in OMC-1, we consider it unlikely that such a rotation of linear polarization is causing the Stokes *V* profile in the present observations, since one would then expect the stronger masers listed in Table 2 to also show significant circular polarization signatures. Yet another effect to consider is the generation of circular polarization by a rotation of the axis of symmetry for the molecular quantum states (Vlemmings et al. 2011). This would occur if the maser stimulated emission rate *R* were to become larger than $g\Omega$, the frequency shift due to the Zeeman effect. The stimulated emission rate *R* is given by

$$R \simeq \frac{AkT_b\Delta\Omega}{4\pi h\nu} \tag{2}$$

(Vlemmings et al. 2011), where *A* is the Einstein coefficient, T_b is the maser brightness temperature, $\Delta\Omega$ is the maser beaming angle, and ν is the frequency of the observed maser transition. We use $A = 5.570 \times 10^{-8}\,s^{-1}$, the highest Einstein coefficient in Lankhaar et al. (2018) for the $\nu = 24959.079 \times 10^6$ Hz CH_3OH maser transition, and $T_b = 10^6$–10^7 K, $\Delta\Omega \simeq 0.03$–0.003 for the 25 GHz maser line (Leurini et al. 2016). Using these values in Equation (2), we obtain $R \leqslant 3 \times 10^{-3}\,s^{-1}$. Meanwhile, $g\Omega \approx 170\ s^{-1}$ in our observations of OMC-1. This means that $R \ll g\Omega$, and thus it is unlikely that a rotation of the axis of symmetry for the molecular quantum states is responsible for the shape of the Stokes *V* profile. Finally, Houde (2014) found that maser radiation scattering off foreground molecules can increase the antisymmetry in the Stokes *V* spectral profile of SiO masers. Consequently, if the Stokes *V* profile were ascribed to the Zeeman effect, one would obtain a much larger value for the magnetic field traced by these SiO masers. While we cannot rule out this effect in our 25 GHz CH_3OH maser observations, our $B_{\rm los}$ values are not orders of magnitude higher than the fields expected in such regions, unlike in SiO masers. We will discuss this in more detail in the next subsection.

4.3. Magnetic Fields and Densities

If the observed Stokes *V* profile is caused by a magnetic field in the source, and is not due to any instrumental effects or other non-Zeeman causes discussed in Section 4.2, then we have a magnetic field from our 25 GHz Class I CH_3OH maser observation of OMC-1 that is three to four times larger (depending on which hyperfine is responsible for the maser) than the highest magnetic field we have detected to date in Class I CH_3OH masers at 44 GHz (Momjian & Sarma 2017). Such a value is not implausible, however; if we assume that the fields are amplified in proportion to the density in the shocked regions where these masers occur, then

$$\frac{B_{\rm post}}{B_{\rm pre}} = \frac{n_{\rm post}}{n_{\rm pre}} \tag{3}$$

where $B_{\rm pre}$ and $B_{\rm post}$ are the magnetic fields in the pre- and post-shock regions respectively, and $n_{\rm pre}$ and $n_{\rm post}$ are the densities in these regions. We can use Equation (3) to calculate $B_{\rm pre}$ and compare it to magnetic fields calculated from other observations. Since our measured fields are in the range 171–214 mG depending on which hyperfine is responsible for the maser transition (Table 3), we will use $B_{\rm post} = 171$ mG in our calculations; this is convenient because $B_{\rm pre}$ values corresponding to $B_{\rm post} = 214$ mG can then be found by multiplying our results by a factor of 1.25. Leurini et al. (2016) have found that bright Class I methanol masers likely occur in regions with densities in the range $10^{7-8}\,cm^{-3}$, so we will calculate $B_{\rm pre}$ corresponding to both $n_{\rm post} = 10^7$ and $10^8\,cm^{-3}$. For densities in the pre-shocked gas we draw upon the work of Kwan et al. (1977), who found that a minimum pre-shock density of $10^5\,cm^{-3}$ is required to produce the observed intensities in the H_2 $\nu = 1-0$ emission lines in OMC-1. Thus, densities in the pre-shocked material of interest are likely of the order of $10^5\,cm^{-3}$ or higher, but unlikely to be as high as, or higher than, $10^6\,cm^{-3}$ (e.g., the references used below in discussing our calculated values for $B_{\rm pre}$). Therefore, we calculate $B_{\rm pre}$ for a range of $n_{\rm pre}$ values from $1.0 \times 10^5\,cm^{-3}$ to $1.0 \times 10^6\,cm^{-3}$. The results of our calculations using Equation (3) are given in Table 4; we find that for a lower post-shock density of $10^7\,cm^{-3}$, the magnetic field in the pre-shock region could be as low as 1.7 mG or as high as 17 mG for the range of pre-shock densities used in our calculation. Meanwhile, if the post-shock density is as high as $10^8\,cm^{-3}$, magnetic fields in the pre-shock region would be lower, and in the range of 0.17 to 1.7 mG. Indeed, Chuss et al. (2019) report magnetic field values of 0.931–1.013 mG in the BN/KL region of OMC-1, where $n = 2.27 \times 10^5\,cm^{-3}$. These magnetic field values were calculated by applying the Chandrasekhar–Fermi

Table 4
Pre-shock Magnetic Fields

n_{post} (cm^{-3})	n_{pre} (cm^{-3})	B_{post} (mG)	B_{pre} (mG)
10^7	1.0×10^5	171	1.71
10^7	2.5×10^5	171	4.28
10^7	5.0×10^5	171	8.55
10^7	7.5×10^5	171	12.8
10^7	1.0×10^6	171	17.1
10^8	1.0×10^5	171	0.17
10^8	2.5×10^5	171	0.43
10^8	5.0×10^5	171	0.86
10^8	7.5×10^5	171	1.28
10^8	1.0×10^6	171	1.71

Table 5
Post-shock Densities

B_{pre} (mG)	n_{pre} (cm^{-3})	B_{post} (mG)	n_{post} (cm^{-3})
0.931[a]	2.27×10^5	171	$10^{7.6}$
1.013[a]	2.27×10^5	171	$10^{7.6}$
0.931[a]	2.27×10^5	214	$10^{7.7}$
1.013[a]	2.27×10^5	214	$10^{7.7}$
6.6[b]	8.3×10^5	171	$10^{7.3}$
6.6[b]	8.3×10^5	214	$10^{7.4}$

Notes.
[a] B_{pre} and n_{pre} taken from Chuss et al. (2019).
[b] B_{pre} and n_{pre} taken from Pattle et al. (2017).

statistical method to their dust polarimetry data taken with the HAWC+ instrument on the Stratospheric Observatory for Infrared Astronomy. Meanwhile, Pattle et al. (2017) calculated a magnetic field of 6.6 mG in gas of density $8.3 \times 10^5\,cm^{-3}$ toward OMC-1, based on polarization measurements as part of the B-fields in the Star-forming Region Observations survey with the James Clerk Maxwell Telescope.

With values for n_{pre} and B_{pre} available from Chuss et al. (2019) and Pattle et al. (2017) for the pre-shock regions of interest in OMC-1, we can also use our detected values of B_{post} in Equation (3) to narrow the range of post-shock densities in which the 25 GHz CH_3OH masers are being excited. The calculated values of n_{post} are given in Table 5. For pre-shocked regions where the densities are $2.27 \times 10^5\,cm^{-3}$ and fields are $\sim$1 mG, we see that 25 GHz Class I CH_3OH masers would be excited in regions of density $10^{7.6}\,cm^{-3}$ if these regions had magnetic fields of 171 mG; n_{post} would be $10^{7.7}\,cm^{-3}$ if the magnetic fields were as high as 214 mG. Meanwhile, if the fields and densities were higher in the pre-shock regions (6.6 mG and $8.3 \times 10^5\,cm^{-3}$ respectively), then the masers would be excited in post-shock regions with densities $10^{7.3}\,cm^{-3}$ if the magnetic field in these regions were 171 mG, or $10^{7.4}\,cm^{-3}$ for post-shock magnetic fields as high as 214 mG. All of these values for n_{post} are in good agreement with densities of $10^{7-8}\,cm^{-3}$ (Leurini et al. 2016) in the post-shock regions in which these 25 GHz Class I CH_3OH masers occur.

4.4. Magnetic Field Values and Energetics

If we accept that the observed Stokes V profile is due to the Zeeman effect, then we obtain that $B_{los} = 171$–214 mG in the regions traced by these 25 GHz Class I CH_3OH masers. As we have noted already, these values are high, about three to four times higher than the largest field we have measured in the 44 GHz Class I CH_3OH maser line (Momjian & Sarma 2017). Yet, as we have demonstrated in Section 4.3, the B_{los} values are not implausibly high. It is possible that these high values for B_{los} could be a consequence of the OMC-1 region being a special case. No other region to date is known to have 25 GHz CH_3OH masers as bright as those in OMC-1. The outflow in Orion-KL is one of the most powerful ever discovered in a star-forming region. In an interesting coincidence, Troland et al. (2016) found from Zeeman effect observations in the thermal lines of H I and OH that magnetic fields in the Orion Veil, a photon-dominated region $\approx$2 pc *in front of* the Trapezium stars in Orion, are three to five times stronger than they are in other regions with comparable values of density. Troland et al. (2016) speculate that the reason for this could lie in the history of OMC-1 before star formation, in that OMC-1 formed in a low-turbulence environment due to its position outside the Galactic plane, and less magnetic flux was removed from the developing cloud.

A central purpose of Zeeman effect observations is to compare the magnetic energy to other relevant energy values in the region being observed. We can use our derived value of B_{los} to find the magnetic energy density and compare it to the kinetic energy density. The magnetic energy density is given by $B^2/8\pi$, where $B^2 = 3B_{los}^2$ (Crutcher 1999). If we use $B_{los} = 171$ mG, we get that the magnetic energy density is equal to $3.5 \times 10^{-3}\,erg\,cm^{-3}$. Meanwhile, the kinetic energy density is given by $(3/2)\,mn\sigma^2$, where m is the mass and σ is the velocity dispersion. This expression for the kinetic energy density includes the contribution of both thermal and turbulent motions. To find the mass, we use $m = 2.8\,m_p$, where m_p is the proton mass; the numerical factor of 2.8 also accounts for the presence of 10% He. The velocity dispersion is related to the FWHM velocity linewidth Δv by $\sigma = \Delta v/(8\ln 2)^{1/2}$. Using the observed FWHM velocity linewidths (0.13–0.53 km s^{-1}; Table 2) of the 25 GHz CH_3OH masers, however, will not yield a representative value of the kinetic energy density in the post-shock region, since masers may have a narrower linewidth than that in the region in which they are formed. We use $\Delta v = 7$ km s^{-1} from observations of the quasi-thermal $10_1 - 9_2$ A^- CH_3OH transition at 23.4 GHz by Wilson et al. (1989). This gives a value of $\sim 3.1 \times 10^{-5}$ erg cm^{-3} for the kinetic energy density in OMC-1, implying the magnetic energy density in the post-shocked gas dominates over the kinetic energy density. A better indicator of the significance of the magnetic field, however, might be to compare it to the pressure in the shock, given by $(1/2)\,\rho\,v^2$, where v is the shock velocity. Using a shock velocity of 30 km s^{-1} (Leurini et al. 2016), we get a pressure of $5.3 \times 10^{-4}\,erg\,cm^{-3}$; the pressure would have a higher value of $1.1 \times 10^{-3}\,erg\,cm^{-3}$ if the post-shock density were as high as $10^{7.7}\,cm^{-3}$. Thus the magnetic energy is of the same order as, or marginally larger than, the pressure in the shock. Therefore, we would expect the magnetic field to play a significant role in shaping the dynamics in these post-shocked regions of OMC-1.

5. Conclusions

We have discovered a signature in the Stokes V profile of a 25 GHz Class I CH_3OH maser toward the high-mass star-forming region OMC-1. If this feature in Stokes V is caused by a

magnetic field in the source and is not due to instrumental effects or other non-Zeeman contributions, then these observations would be the first detection and discovery of the Zeeman effect in the 25 GHz Class I CH_3OH maser line. We find that z $B_{los} = 152 \pm 12$ Hz from our first epoch of observations in 2009 in the *D*-configuration of the VLA, and z $B_{los} = 149 \pm 19$ Hz from our second epoch of observations in 2017 in the *C*-configuration of the VLA, very likely for the same maser spot. The agreement in magnetic field strengths over observations taken 8 yr apart with different angular resolutions is remarkable. Based on which one of four hyperfines is masing, these values correspond to magnetic fields in the range 171–214 mG; there are four other hyperfines that we exclude because the B_{los} yielded by them would be unreasonably high for the regions in which these masers occur. Our detected values of B_{los} are nevertheless high, about three to four times higher than the strongest field we have measured in 44 GHz Class I CH_3OH masers. Yet, they are not implausible. For a density of 10^7 cm^{-3} in the post-shock regions in which the 25 GHz Class I CH_3OH masers occur, $B_{los} = 171$ mG corresponds to a pre-shock field of 1.7 mG in a region of density 1.0×10^5 cm^{-3}. Even if densities were higher, 1.0×10^6 cm^{-3} for the pre-shock region and 10^8 cm^{-3} for the post-shock region respectively, the magnetic field in the pre-shock region would still be 1.7 mG. Conversely, if fields and densities in the pre-shock regions were 0.9–1.0 mG and 2.27×10^5 cm^{-3} respectively, as observed by Chuss et al. (2019), then a post-shock field of 171 mG would imply a region of density $10^{7.6}$ cm^{-3}. It is in regions with densities 10^{7-8} cm^{-3} that 25 GHz Class I CH_3OH masers are believed to occur. Thus, the higher B_{los} values we have measured may be due to the OMC-1 region being special; this includes OMC-1 having the brightest known 25 GHz Class I CH_3OH masers. Finally, our detected values of B_{los} indicate that the magnetic energy will dominate over the kinetic energy, even if the FWHM linewidth in these regions is as broad as 7 km s^{-1}. Also, the magnetic energy is at least of the same order, and perhaps slightly higher in value, than the pressure in the shock. Therefore, the magnetic field is likely important in shaping the dynamics in the post-shocked regions where these masers occur.

We would like to thank an anonymous referee for comments that have helped in improving the final manuscript.

Facility: VLA.

ORCID iDs

A. P. Sarma https://orcid.org/0000-0001-6590-552X
E. Momjian https://orcid.org/0000-0003-3168-5922

References

Bally, J. 2008, in Handbook of Star Forming Regions, ed. Bo. Reipurth, Vol. I (San Francisco, CA: ASP), 459
Bally, J., Langer, W. D., Stark, A. A., et al. 1987, ApJL, 312, L45
Barrett, A. H., Schwartz, P. R., & Waters, J. W. 1971, ApJL, 168, L101
Becklin, E. E., & Neugebauer, G. 1967, ApJ, 147, 799
Beckwith, S., Persson, S. E., Neugebauer, G., et al. 1978, ApJ, 223, 464
Chuss, D. T., Andersson, B.-G., Bally, J., et al. 2019, ApJ, 872, 187
Crutcher, R. M. 1999, ApJ, 520, 706
Crutcher, R. M. 2012, ARA&A, 50, 29
Erickson, N. R., Goldsmith, P. F., Snell, R. L., et al. 1982, ApJL, 261, L103
Genzel, R., & Stutzki, J. 1989, ARA&A, 27, 41
Greisen, E. W. 2003, ASSL, 285, 109
Greisen, E. W. 2015, in AIPS Memo, 118, http://www.aips.nrao.edu/aipsmemo.html
Hacar, A., Tafalla, M., Forbrich, J., et al. 2018, A&A, 610, A77
Houde, M. 2014, ApJ, 795, 27
Johnston, K. J., Gaume, R., Stolovy, S., et al. 1992, ApJ, 385, 232
Johnstone, D., & Bally, J. 1999, ApJL, 510, L49
Kleinmann, D. E., & Low, F. J. 1967, ApJL, 149, L1
Kounkel, M., Hartmann, L., Loinard, L., et al. 2017, ApJ, 834, 142
Krumholz, M. R., & Federrath, C. 2019, FrASS, 6, 7
Kwan, J. H., Gatley, I., Merrill, K. M., et al. 1977, ApJ, 216, 713
Lankhaar, B., Vlemmings, W., Surcis, G., et al. 2018, NatAs, 2, 145
Leurini, S., Menten, K. M., & Walmsley, C. M. 2016, A&A, 592, A31
Menten, K. M. 1993, LNP, 412, 199
Momjian, E., & Sarma, A. P. 2017, ApJ, 834, 168
Momjian, E., & Sarma, A. P. 2019, ApJ, 872, 12
Motte, F., Bontemps, S., & Louvet, F. 2018, ARA&A, 56, 41
Pabst, C., Higgins, R., Goicoechea, J. R., et al. 2019, Natur, 565, 618
Pattle, K., Ward-Thompson, D., Berry, D., et al. 2017, ApJ, 846, 122
Sarma, A. P., & Momjian, E. 2009, ApJL, 705, L176
Sault, R. J., Killeen, N. E. B., Zmuidzinas, J., & Loushin, R. 1990, ApJS, 74, 437
Troland, T. H., & Crutcher, R. M. 2008, ApJ, 680, 457
Troland, T. H., Goss, W. M., Brogan, C. L., et al. 2016, ApJ, 825, 2
Troland, T. H., & Heiles, C. 1982, ApJ, 252, 179
Vlemmings, W. H. T., Torres, R. M., & Dodson, R. 2011, A&A, 529, A95
Wiebe, D. S., & Watson, W. D. 1998, ApJL, 503, L71
Wilson, T. L., Johnston, K. J., Henkel, C., et al. 1989, A&A, 214, 321